Photodegradation of *2,4*-dichlorophenoxyacetic acid over TiO_2(B)/anatase nanobelts and Au-TiO_2(B)/anatase nanobelts

A. Chenchana[(1,2)], A. Nemamcha[(1)], H. Moumeni[(1)], J.M. Doña Rodríguez[(2)], J. Araña[(2)], J.A. Navío[(3)], O. González Díaz*[(2)], E. Pulido Melián*[(2)]

[(1)]Equipe: Surfaces, Interfaces et Nanostructures, Laboratoire d'Analyses Industrielles et Génie des Matériaux, Université 8 Mai 1945, Guelma, Guelma 24000, Algeria.

[(2)]Grupo de Fotocatálisis y Espectroscopía para Aplicaciones Medioambientales (Unidad Asociada al CSIC). Dpto. Química. Instituto de Estudios Ambientales y Recursos Naturales (i-UNAT), Universidad de Las Palmas de Gran Canaria. Campus Universitario de Tafira, 35017, Las Pa lmas. Spain.

[(3)]Instituto de Ciencia de Materiales de Sevilla, Centro Mixto Universidad de Sevilla-CSIC, Américo Vespucio 49, 41092 Sevilla, Spain

Corresponding authors: E. Pulido Melián (elisenda.pulido@ulpgc.es), O. González Díaz (oscar.gonzalez@ulpgc.es)

Abstract

In this work, novel TiO_2-based nanobelts with various phases were synthesized: biphasic TiO_2(B)/anatase, pure TiO_2(B) and pure anatase. These catalysts were obtained via hydrothermal reaction using two nanoparticulated TiO_2 photocatalysts as precursors: Aeroxide TiO_2 P25 (P25) and TiO_2 synthesized via a sol-gel process (SG). In addition, the surface of the photocatalysts was modified with gold using a photodeposition method. A characterization study of the different photocatalysts was performed with X-ray diffraction analysis (XRD), UV-Vis diffuse reflectance spectra (DRS), scanning electron microscopy (SEM), X-ray photoelectron spectrum analysis (XPS) and Brunauer-Emmett-Teller measurements (BET). The photocatalytic reaction of the herbicide *2,4*-dichlorophenoxyacetic acid (2,4-D) was investigated under UVA irradiation. A toxicity analysis was performed with the marine bioluminescent bacteria *Vibrio fischeri*. The highest 2,4-D removal efficiency of 99.2% was obtained with the biphasic Au-TiO_2(TiO_2(B)/anatase) nanobelts with anatase as predominant phase. Toxicity was mainly due to the intermediate *2,4*-dichlorophenol (*2*,4-DCP) which was eliminated in 4 h. The TiO_2 nanobelt phase structure is shown to have a significant effect on photocatalytic activity.

Keywords

Au-TiO_2 (TiO_2(B)/anatase) nanobelts, hydrothermal, sol-gel process, heterogeneous photocatalysis.

1. Introduction

The excessive use of pesticides to increase agricultural production and contribute to covering the growing demand for food has led to the agricultural sector being considered a major worldwide source of water pollution. Pesticides, such as the agrochemical *2,4*-dichlorophenoxyacetic acid (2,4-D), have negative effects on human health and aquatic ecosystems, contaminating ground waters and surface waters. It has been reported that 2,4-D can seriously alter soil water quality and contaminate surface waters, adversely affecting human and animal life due to its disruptive effect on the hormonal system and its potential carcinogenic effects [1].

The most promising method for the decomposition of 2,4-D herbicides is by heterogeneous photocatalysis. The photocatalytic processes are based on absorption of photons by a semiconductor material whose energy is higher than the band gap energy, E_g, allowing the formation of an electron-hole pair (e^-/h^+) in the semiconductor [2]. The interfacial transfer of electrons and holes in the semiconductor results in the initiation of redox reactions with adsorbates [3].

Titanium dioxide (TiO_2) has been widely investigated as a semiconductor material due to its high photocatalytic activity and chemical stability [4,5]. Generally, the phase structure and the morphology of a TiO_2 catalyst play important roles in its photocatalytic performance. Anatase and rutile are generally considered the most efficient phases for the photocatalytic process, although in nature there exist four distinct polymorphs: anatase, rutile, brookite, and monoclinic TiO_2 (TiO_2 (B)) [6]. With the exception of anatase and rutile, phase mixtures have not been studied in depth. In this respect, the commercial Aeroxide TiO_2 P25 (P25) is a mixed phase catalyst (80% anatase and 20% rutile) and has displayed excellent photocatalytic activity in the elimination of different pollutants [7]. With respect to morphological structure, many scientific articles have focused on the efficient removal from water of the herbicide 2,4-D, using, for this purpose, different photocatalytic structures, such as the thin plate structure [8], nanospheres [9] and nanotubes [10]. Recent research studies have concentrated on a novel TiO_2 nanostructure morphology, one-dimensional (1D) nanobelts. These structures have intriguing potential, as they can be used in a variety of applications, including lithium batteries [11,12], sensors [13,14], hydrogen production [15,16] and its storage [17,18], solar cells [19,20] and photocatalysis [21,22].

In this work, TiO_2 nanobelts were obtained by subjecting the commercial Aeroxide TiO_2 P25 (P25) and a home-made TiO_2 synthesized in our laboratory to a sol-gel process and hydrothermal treatment. The samples obtained were subjected to several calcination temperatures, and the best-performing nanobelt photocatalysts were modified by surface photodeposition with Au nanoparticles. Photocatalytic activities were tested in the degradation of the herbicide 2,4-D and its main, most toxic intermediate, 2,4-DCP (*2,4*-dichlorophenol), which is considered even more toxic than the parent pollutant 2,4-D [2]. All photocatalysts were widely characterized by various physicochemical techniques (XRD, UV-Vis diffuse reflectance, BET, XPS, FTIR, TEM and SEM-EDX).

2. Experimental

2.1 Materials

Aeroxide TiO_2 P25 (P25) was obtained from Evonik Industries. Sodium hydroxide 98.0%$_{wt}$ (NaOH), hydrochloric acid 37%$_{wt}$ (HCl), ethanol absolute 99.5%$_{wt}$ (CH_3CH_2OH), anhydrous citric acid 99.5%$_{wt}$ ($C_6H_8O_7$), and sodium chloride 99.5%$_{wt}$ (NaCl) were purchased from Panreac Quimica S.A. (Barcelona, Spain). Titanium (IV) *n*-butoxide 97%$_{wt}$, *2,4*-dichlorophenoxyacetic acid 97%$_{wt}$ ($C_8H_6Cl_2O_3$), tetrachloroauric acid trihydrate 99.9%$_{wt}$ ($HAuCl_4 \cdot 3H_2O$) and *2*-propanol 99.8%$_{wt}$ were obtained from Sigma-Aldrich. Bacteria *Vibrio fischeri* (aliivibrio fischeri) were purchased from Gomensoro S.A. (Madrid, Spain).

2.2 Preparation of TiO_2 nanoparticles with sol-gel procedure

In the first step, a mixture of ethanol (40 mL) and titanium (IV) n-butoxide (17 mL) was added drop by drop to a water-ethanol solution (15 mL of water and 40 mL of ethanol) containing 853 mg of citric acid. The solution was constantly stirred during the whole process. Subsequently, the suspension was stirred for an additional 30 minutes and then kept in the dark for 48 h. Finally, the gel was dried at 100°C for 24 h. The obtained powder was named SG [23].

2.3 Preparation of TiO_2 nanobelts

The nanobelts were synthesized by our group either directly by hydrothermal treatment of the P25 photocatalyst (HP25 series) or of the SG photocatalyst (SGH series). A typical synthesis process involved 1 g of TiO_2 mixed with 140 mL of 10 M NaOH aqueous solution. The mixed solution was magnetically stirred until the solution could be homogeneously suspended, then transferred into a Teflon vessel with cap which was introduced into a stainless steel autoclave heated at 180°C for 48 h. The obtained liquid was isolated by centrifugation at 4000 rpm for 30 min, washed with 140 mL of Milli-Q water and centrifuged again for 30 min, followed by a filtration process and 3 washes with 140 mL of Milli-Q water to obtain $Na_2Ti_3O_7$. The wet powder was then immersed in 140 mL of 0.1 M HCl aqueous solution for 24 h with continuous magnetic stirring. After washing and filtration $H_2Ti_3O_7$ nanobelts were produced and then dried at 105°C for 24 h [24]. Finally, the powder was calcined at different temperatures (500°C, 600°C, 700°C) for 3.5 h.

2.4 Preparation of Au/TiO_2

Au nanoparticles were deposited on the TiO_2 nanobelt surface using the photodeposition method [25]. Appropriate solutions of $HAuCl_4 \cdot 3H_2O$ (amount calculated for 1%wt Au) and 2 g of TiO_2 (HP25 or SGH) nanobelts were added to a mixture solution containing 400 mL of Milli-Q water and 9.4 mL of *2*-propanol. Photodeposition was performed using a cylindrical photoreactor with a 400 W Hg medium pressure lamp enclosed inside a quartz inner tube. The mixture was illuminated for 6 h under continuous stirring and nitrogen bubbling. The obtained product was thoroughly recovered by filtration using a 0.45 μm Millipore filter, washed with Milli-Q water and oven dried at 105°C for 24 h.

2.5 Characterization techniques

X-ray diffraction (XRD) patterns were obtained using a Bruker D8 Advance diffractometer with Cu Kα radiation 1.5406 Å in the 2θ scan range of 15-60°.

Field emission scanning electron microscopy (SEM) images were obtained using a Hitachi TM3030 microscope equipped with an EDX analyzing system, and transmission electron microscopy (TEM) images using a Zeiss EM 910 instrument equipped with a ProScan slow-scan CCD camera and Soft Imaging System software.

Diffuse reflectance UV-Vis spectra (DRS-UV-Vis) were recorded on a Varian Cary 5 spectrophotometer using PTFE (Poly-Tetra-Fluoroethylene) as reference. The band gap energy was calculated according to the Tandon-Gupta method [26].

BET surface area and porosity measurements were carried out by N_2 adsorption at 77 K using a Micromeritics ASAP 2010 instrument.

Surface characterization by X-ray photoelectron spectroscopy (XPS) was conducted on a Leybold-Heraeus LHS-10 spectrometer, working with constant pass energy of 50 eV. The spectrometer main chamber was maintained at a pressure $<2\cdot10^{-9}$ Torr, and the machine was equipped with an EA-200 MCD hemispherical electroanalyzer with a dual X-ray source of Al Kα (hν) 1486.6 eV at 120 W and 30 mA. Samples were outgassed in the pre-chamber of the instrument at 150°C up to a pressure <2·10-8Torr to remove chemisorbed water from their surfaces.

FTIR experiments were carried out with a Nicolet iS10 spectrophotometer and a custom-made cell equipped with CaF_2 windows. The samples were analyzed under the following parameters: intervals of 4000-1000 cm^{-1}, a 4 cm^{-1} resolution with 32 scans and a mirror velocity of 0.6329 $cm\cdot s^{-1}$.

2.6 Photodegradation of 2,4-D

Aqueous suspensions containing 0.53 mM of 2,4-D aqueous solution and 1 $g\cdot L^{-1}$ photocatalyst were placed in a 250 mL Pyrex cylindrical reactor [2]. The photodegradation experiments were carried out at room temperature at pH 3, with continuous stirring and air-bubbling (air flow = 400 $mL\cdot min^{-1}$). In order to achieve the adsorption-desorption equilibrium between the organic pollutant and the photocatalysts, the suspensions were magnetically stirred and bubbled in the dark for 30 min at room temperature. Subsequently, an aliquot was taken and filtered with a syringe filter (0.45 µm) and injected into the high-performance liquid chromatographer (HPLC) and total carbon analyzer to determine the initial instant concentrations of the contaminant and total organic carbon (TOC), respectively. After dark adsorption, the lamp was switched on to start the photocatalytic reaction for 120 min. A 60 W Philips HB175 solarium equipped with four 15 W Philips CLEO fluorescent tubes with emission spectrum from 300 to 400 nm (maximum around 365 nm, and 9 $mW\cdot cm^{-2}$) was used as UVA source of photons for the photocatalytic processes. Sample monitoring in the photocatalysis was carried out in the same way as at the end of the dark period.

2.7 Analytical procedures

The concentration of 2,4-D was evaluated by HPLC. The chromatographic column used was a Supelco Discovery C18 (250 mm x 4.6 mm ID, 5 µm particles), with mobile phase

consisting of 70% methanol and 30% phosphoric acid buffer at pH 2.3. Mineralization was determined using a total carbon analyzer (TOC-VCSN, Shimadzu). A Dionex LC25 chromatography unit equipped with GP50 pump and ED50 electrochemical detector in conductivity mode was used to determine chloride concentration.

2.8 Toxicity measurements*: Vibrio fischeri* toxicity bioassay

A luminescent bacteria test was performed to evaluate toxicity of the herbicide 2,4-D in aqueous solution. The bioassay used marine bioluminescent bacteria of the *Vibrio fischeri* type. The bacteria were hydrated by adding an adequate volume of solution at 2% NaCl by weight prior to testing. For each sample, the NaCl content was 2% (w/v), and luminescence intensity was recorded after 15 minutes of incubation at 35°C. Percentage inhibition was calculated by comparing a non-toxic substance containing only *Vibrio fischeri* bacteria in 2% NaCl saline medium as reference.

3. Results and discussion

3.1 X-ray diffraction (XRD)

Table 1. XRD characterization and band-gap values of the photocatalysts.

Photocatalysts	Phases, %			Crystallite size, nm			Crystallinity %	Band-gap eV
	Monoclinic	Anatase	Rutile	Monoclinic	Anatase	Rutile		
P25	--	83	17	--	19.45	30.48	83	3.2
SG (amorphous)	--	--	--	--	--	--	n.m.	--
HP25-500°C	100	--	--	n.m.	--	--	59	3.07
HP25-600°C	36	64	--	n.m.	n.m.	--	81	3.18
HP25-700°C	--	99	1	--	47.2	137.2	89	3.20
SGH-500°C	80	20	--	n.m.	--	--	81	3.10
SGH-600°C	61	39	--	21.8	19.1	--	82	3.15
SGH-700°C	--	100	--	--	42.2	--	91	3.20
Au-HP25-600°C	37	63	--	21.2	n.m.	--	82	3.17
Au-SGH-600°C	67	33	--	n.m.	n.m.	--	82	3.13

n.m.: not measured.
-- : not present.

The structures of the TiO_2 nanobelts were investigated using the XRD technique. Table 1 shows the results of crystalline phase composition, percentage of crystallinity and

crystallite sizes for several calcination temperatures without and with surface modification by gold nanoparticles for the two HP25 and SGH series. Crystallite size was obtained by applying the Scherrer equation in cases where there was no overlap between peaks. If there was an overlap it is indicated in the table as 'n.m.'.

In the case of the HP25 series, the samples calcined at 500°C contain a pure phase of monoclinic TiO_2(B) which may be due to calcination of the $H_2Ti_3O_7$ structure [27]. The main peak of monoclinic TiO_2(B) is located at 45° (2θ) [PDF 35-0088]. After heating at 600°C, a mixture of phases can be observed, monoclinic TiO_2(B) and anatase phase [PDF 21-1272]. In this sample, the transformation from monoclinic TiO_2(B) to anatase phase was initiated, with anatase the predominant phase (denoted TiO_2(A/B)). This mixture had 36% TiO_2(B) and 64% anatase. At 700°C, TiO_2(B) was transformed almost completely to anatase structure (99%), with a small percentage of rutile phase (1%) [PDF 21-1276]. This sample exhibited higher crystallinity.

For the SGH series, it was found that the mixture of TiO_2(B) and anatase phase appeared in the sample calcined at 500°C. When the temperature was increased to 600°C, a slow transformation of TiO_2(B) into anatase structure was observed, with the TiO_2(B) phase remaining predominant (denoted TiO_2(B/A)). At this calcination temperature, anatase phase was just 39% in contrast to the 64% anatase structure of the HP25-600. Pure anatase phase was obtained with the sample obtained at 700°C, which exhibited the highest crystallinity of 91%. Transformation from anatase to rutile phase did not occur at 700°C for the SGH series, though this transformation did begin with the HP25-700.

The results obtained appear to indicate that the non-calcined SG sample is amorphous, and so the hydrothermal process causes delay of phase transformation from TiO_2(B) to anatase. This phase transformation is achieved as the calcination temperature increases. Rutile phase is not detected in this series, even at 700°C. The phase transformations from TiO_2(B) to anatase and from anatase to rutile took place rapidly in the HP25 series. Nevertheless, the original commercial photocatalyst, P25 (before hydrothermal treatment), has a crystalline structure formed by nanoparticles with a more or less bipyramidal structure (tetragonal system).

Figure 1 (a) and (b) show the XRD patterns of the samples of both series of photocatalysts without and with modification of photodeposited Au. Diffraction peaks corresponding to Au were not detected. The presence of Au particles did not produce any modification of the crystalline structure of the material.

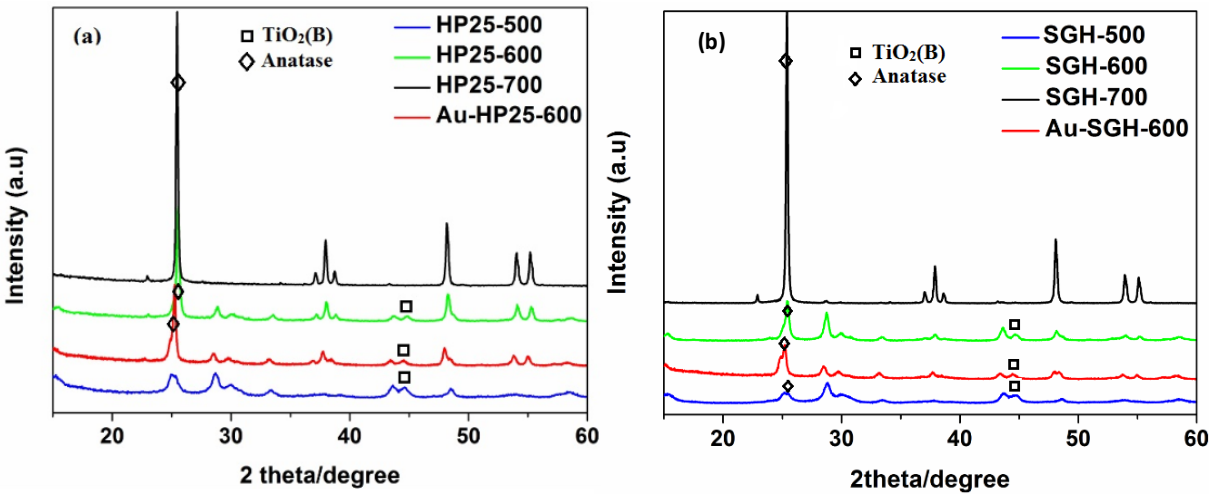

Figure 1. XRD patterns of TiO_2 nanobelt samples: (a) HP25 series and Au-HP25-600, (b) SGH series and Au-SGH600.

3.2 FTIR Spectroscopy analysis

Figure 2 (a) shows the spectra of the reference P25, HP25-500, HP25-600 and HP25-700 catalysts. The bands at 3400 cm^{-1} and 1630 cm^{-1} are attributed to vibrations of the water stretching and bending modes [28]. A decrease in the intensity of these bands is clearly observed as calcination temperature increases.

In the HP25-500 and HP25-600 catalysts, a 983 cm^{-1} band can be seen that is not observed in either the P25 or HP25-700. It is in this region where the characteristic vibrations of the Ti-O appear [29]. This is a broad band associated with changes in the position and intensity of absorption bands characteristic of anatase due to the transformation to TiO_2-B (monoclinic) and reflects the role of the hydrothermal treatment and subsequent acid washing in the introduction of H and OH groups to the TiO_2 structure [30].

The characteristics of the spectra of the SGH catalysts (Fig. 2b) are the same as those of the HP25, with lower surface hydroxylation as temperature increases and the presence of the band increase to 983 cm^{-1} in the catalysts treated at 500ºC and 600ºC. The Au-modified photocatalysts, Au-HP25-600 and Au-SGH-600, display the same behavior.

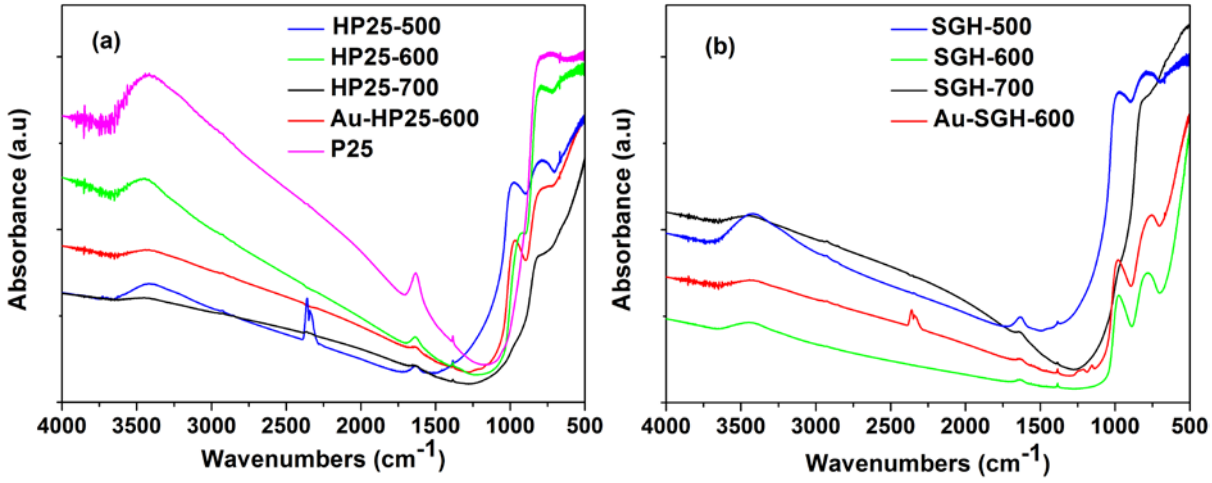

Figure 2. FTIR of nanobelt photocatalysts (a) HP25 series, and (b) SGH series.

After photocatalyst surface characterization through the FTIR spectra, a study was performed aimed at explaining the interactions between the tested pollutant and the active centers of the surface of the catalysts. First, the reference spectra of the photocatalyst samples and pollutants were recorded. The catalysts were then suspended in a saturated solution of the pollutant and, after filtration, their spectra were recorded. Finally, they were subjected to UVA irradiation to follow the evolution over time of the bands resulting from interaction of the 2,4-D with the catalysts.

Figures 3 (a) and (b) show the spectra obtained from interaction of the 2,4-D with the catalysts. Also shown, for purposes of comparison, is the spectrum of the water-dissolved 2,4-D. Table 2 shows the main bands of the 2,4-D. As can be seen in the spectra of the P25 and SGH-600 (Fig. 3 (a)), the band attributed to the vibration ν(C=O) disappears and a widening of the bands is observed in the region between 1500-1400 cm^{-1}. This may be due to the formation of a monodentate or bidentate carboxylate group connected to the catalyst surface. In these photocatalysts, displacement of the 2,4-D acid to its dissociated form is favored.

In the spectra obtained with the HP25-600 and the catalysts photodeposited with gold (Au-HP25-600 and Au-SGH-600), the band corresponding to the carbonyl group is observed together with the widening due to carboxylate formation. With these photocatalysts, interaction of the pollutant with the catalyst surface seems to take place with the two species formed from dissociation of the acid (pK_a 3.40) [31], the molecular species and the anionic (carboxylate) species. Scheme 1 represents the two types of possible interaction observed.

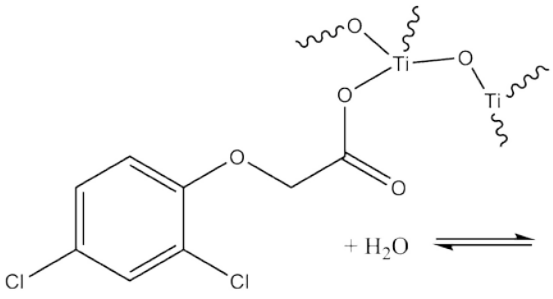

pK_a = 3.40 (25°C)

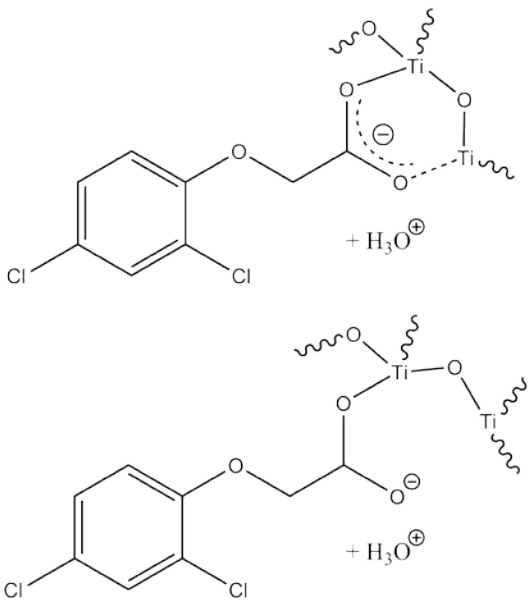

Predominant interactions in P25 and SG-HT

Scheme 1. Interaction of 2,4-D molecule with catalysts.

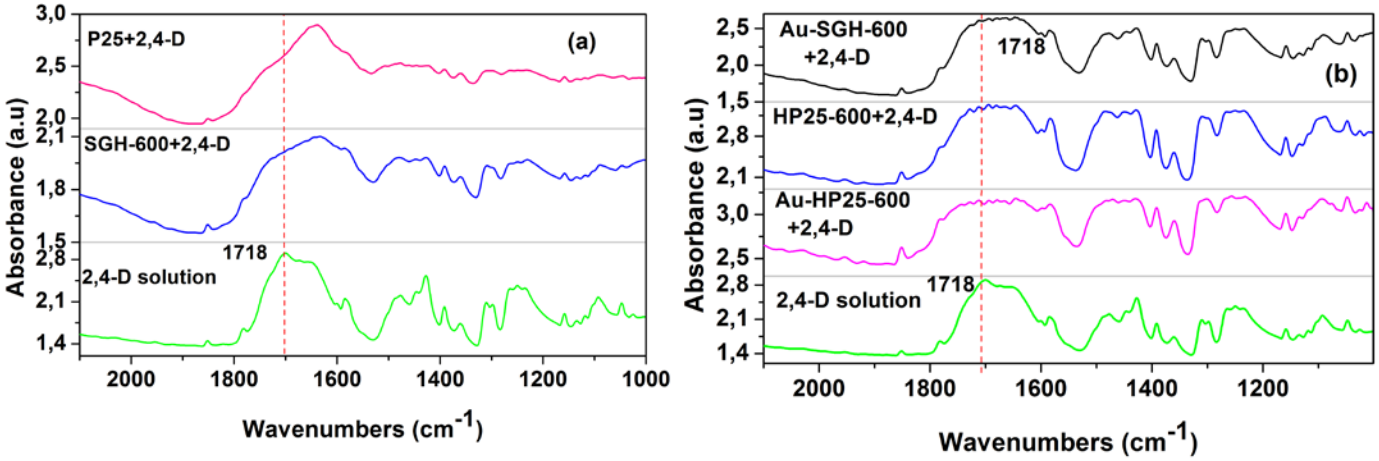

Figure 3 (a) and (b): FTIR spectra of the interaction of 2,4-D with photocatalysts without UVA irradiation.

Table 2. Assignments of the main FTIR bands of 2,4-D

Band (cm^{-1})	Assignment
1718	ν(C=O)
1580, 1475	ν(C=C)
1310, 1092	ν_s and ν_{as}(C-O-C)
1422	CH_2

3.3 Diffuse reflectance UV-Vis spectra

The band gap was estimated using UV-Vis spectra of TiO_2 nanobelts obtained at different calcination temperatures, and was calculated following the procedure described by Tandon and Gupta [26]. In Figure 4, Tauc plots are shown for both series of photocatalysts, with and without Au particle photodeposition. Band gap values are very similar for the SGH and HP25 series.

It can be seen in Table 1, in both series, how the band gap progressively increases with increasing anatase percentage and increasing temperature. This tendency is commonly observed in other studies [32,33] and is attributed to phase transformation of TiO_2(B) to anatase structure by heating at high temperature leading to an interphase charge transfer between the band structure of the TiO_2(B) and anatase. Although the phase transformation of TiO_2(B) to anatase is faster in the HP25 series, no significant differences are observed in the band gap values of the two series. It is also seen how the presence of gold particles has very little effect on the band gap values. The only effect observed is an elevation of the background

signal in the Tauc plots that is clearly noticeable throughout the visible region and that could be associated with the possible presence of plasmons [34,35].

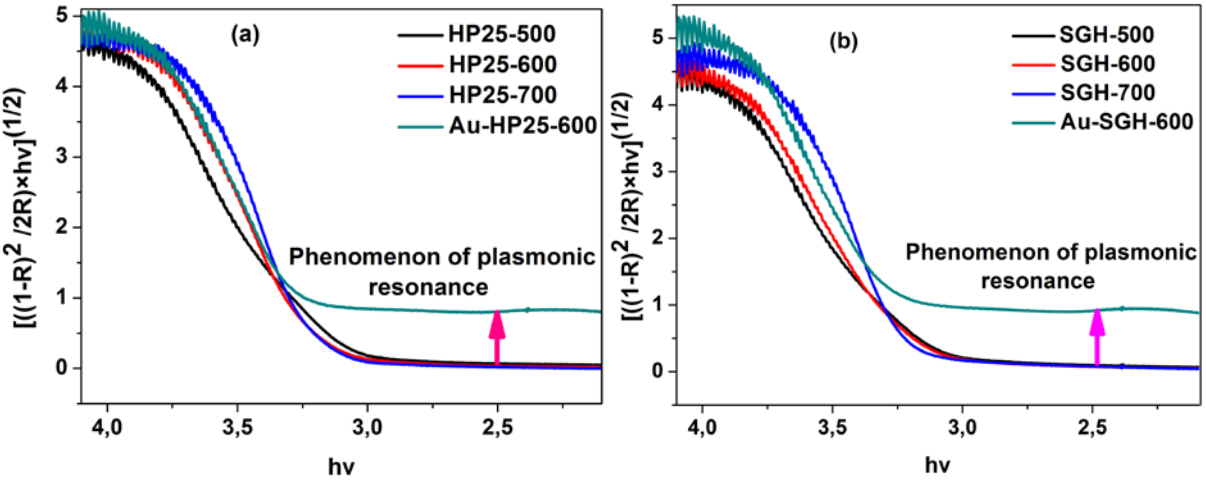

Figure 4. Tauc plots of the TiO_2 nanobelts calcined at different temperatures: (a) HP25 and (b) SGH.

3.4 Electron microscopy

Scanning electron microscopy (SEM) was used to study the morphology of the TiO_2 nanobelts calcined at different temperatures. Figure 5 shows that the prepared samples had a homogeneous nanobelt structure. The nanobelt structures are greater at higher temperatures. This can be seen in greater detail in the TEM images shown in Figure 6. Evolution of the two series, HP5 and SGH, is similar. Images shown of the nanobelts obtained from the P25 reveal how the increase in temperature produces particle sinterization and hence nanobelt growth. The EDX analysis also confirmed that the presence of gold does not appear to be homogenously distributed.

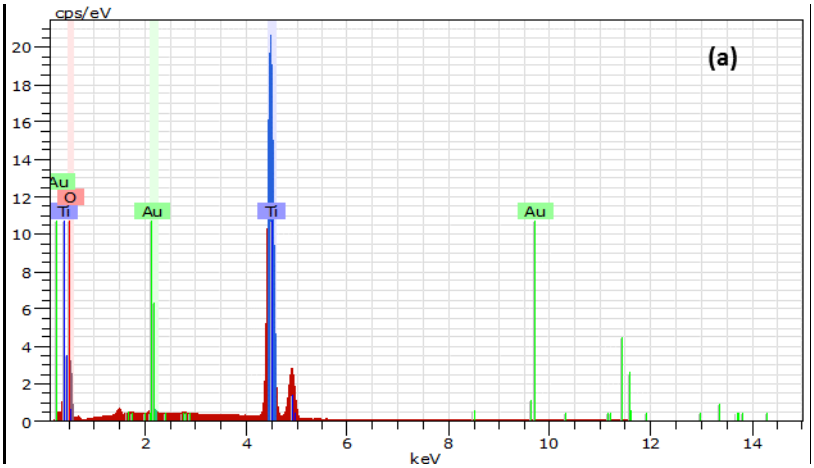

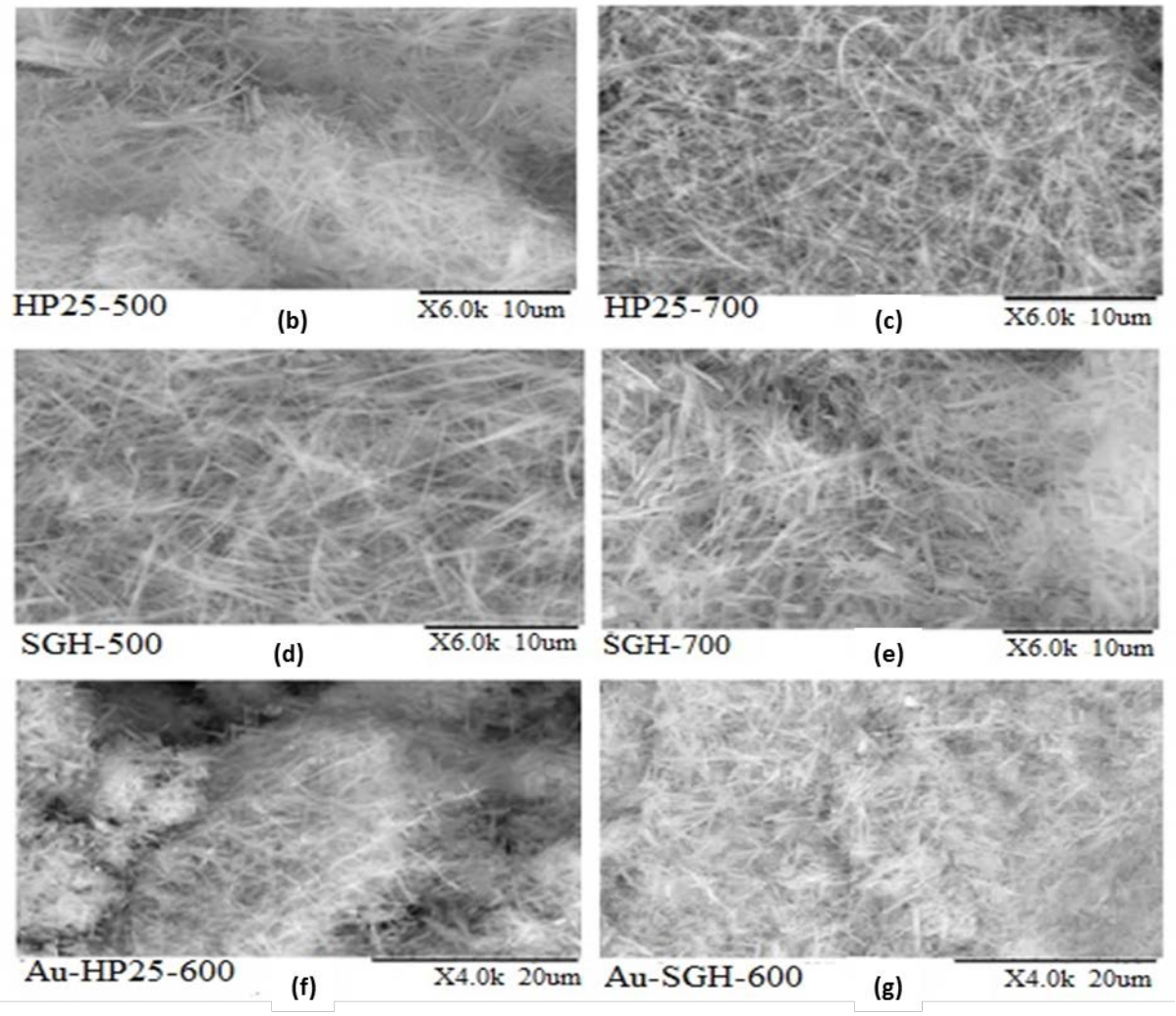

Figure 5. (a) EDX analysis of Au-nanobelts; SEM micrographs: (b) and (c) samples of HP25 calcined at 500ºC and 700°C, respectively; (d) and (e) samples of SGH calcined at 500ºC and 700°C, respectively; (f) HP25 with 1% Au calcined at 600°C; and (g) SGH with 1% Au calcined at 600°C.

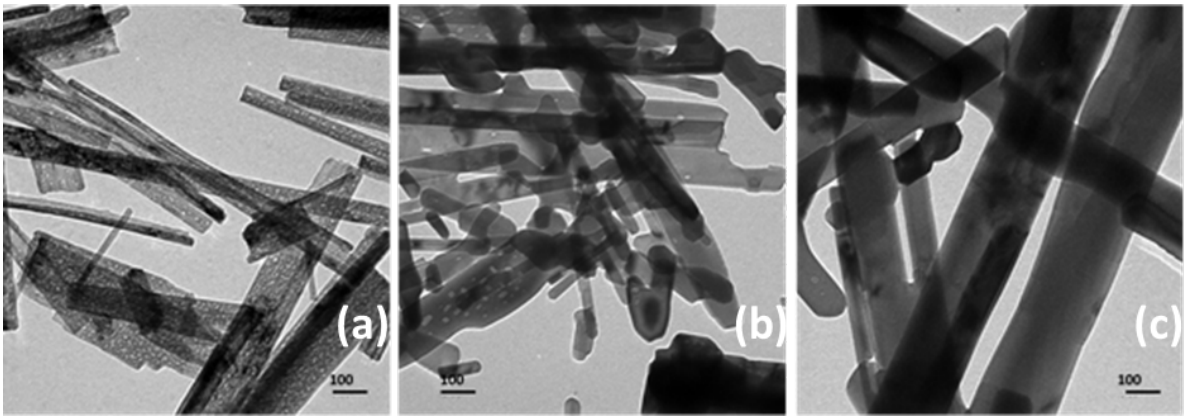

Figure 6. TEM images (a) HP25-500, (b) HP25-700 and (c) HP25-900**.**

3.5 BET analysis

The BET analysis results of the samples are summarized in Table 3. It can be observed that the pure TiO_2 nanobelts have surface areas of 21.85 $m^2 \cdot g^{-1}$ and 23.12 $m^2 \cdot g^{-1}$ for HP25-600 and SGH-600, respectively, with these areas being similar to those found by other authors with different nanobelt photocatalysts [36,37]. After modification with Au nanoparticles, a slight increase in the specific surface area is observed for both series.

In Figure 7, the adsorption-desorption isotherms of N_2 are shown for both series of photocatalysts with and without surface photodeposited Au. It is observed that there is virtually no hysteresis cycle, which indicates that the materials are practically non-porous (pore volumes are shown in Table 3).

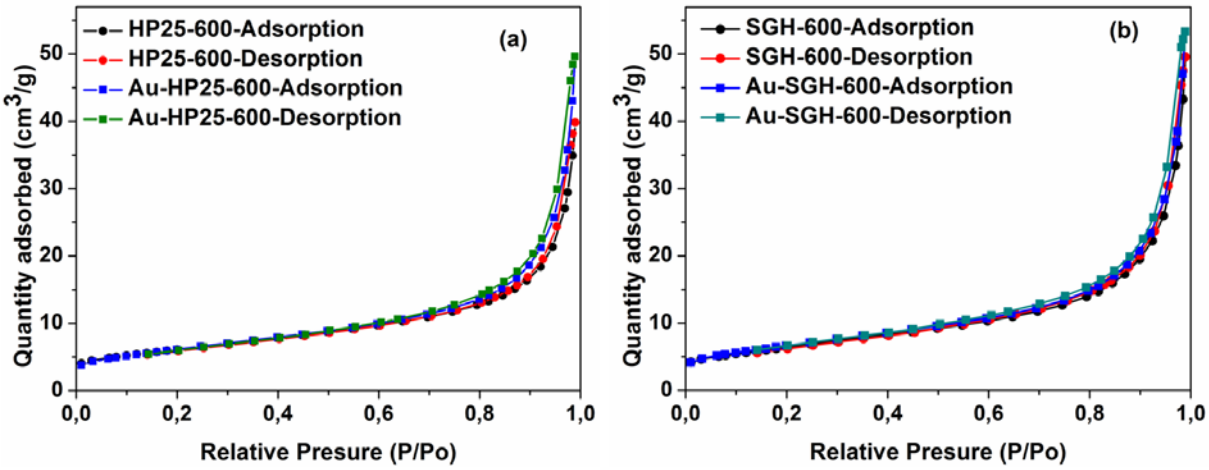

Figure 7. N_2 adsorption/desorption isotherms: (a) HP25-600 and Au-HP25-600, (b) SGH-600 and Au-SGH-600

3.5 X-ray photoelectron spectroscopy (XPS) analysis

XPS measurements were performed to analyze the chemical surface composition. Figure 8 shows the XPS spectra of Ti *2p*, C *1s*, O *1s* and Au *4f*. All these samples have two peaks located at 458.8 eV and attributed to typical values of Ti $2p^{3/2}$ and $2p^{1/2}$, respectively, which correspond to the Ti^{4+} oxidation state of the TiO_2. In Figure 8, the Au *4f* spectrum is comprised of two bending energies of the Au $4f^{7/2}$ and Au $4f^{5/2}$ peaks centred at 83.9 eV ($4f^{7/2}$) and 87.5 eV (Au $4f^{5/2}$), confirming that gold in the metal is in zero oxidation state, Au^o [38]. This involves the existence of an Au-TiO_2 Schottky barrier interface, allowing electron transfer from TiO_2 nanobelts to the Au [39]. Figure 8 shows the spectrum of O *1s* with bending energies values located at 529.7 eV, ascribed to the lattice oxygen O_2 but also assignable to the presence of H_2O or the free hydroxyl group (OH) on the surface. The C *1s* peaks located at 285.9 and 286.2 corresponding to C-C were not detected with FTIR spectroscopy. According to the quantitative analysis shown in Table 3, carbon content is highly significant. The presence of carbon is likely due to possible carbonation of NaOH used in the hydrothermal treatment which was not totally neutralized in the subsequent treatment with HCl aqueous solution.

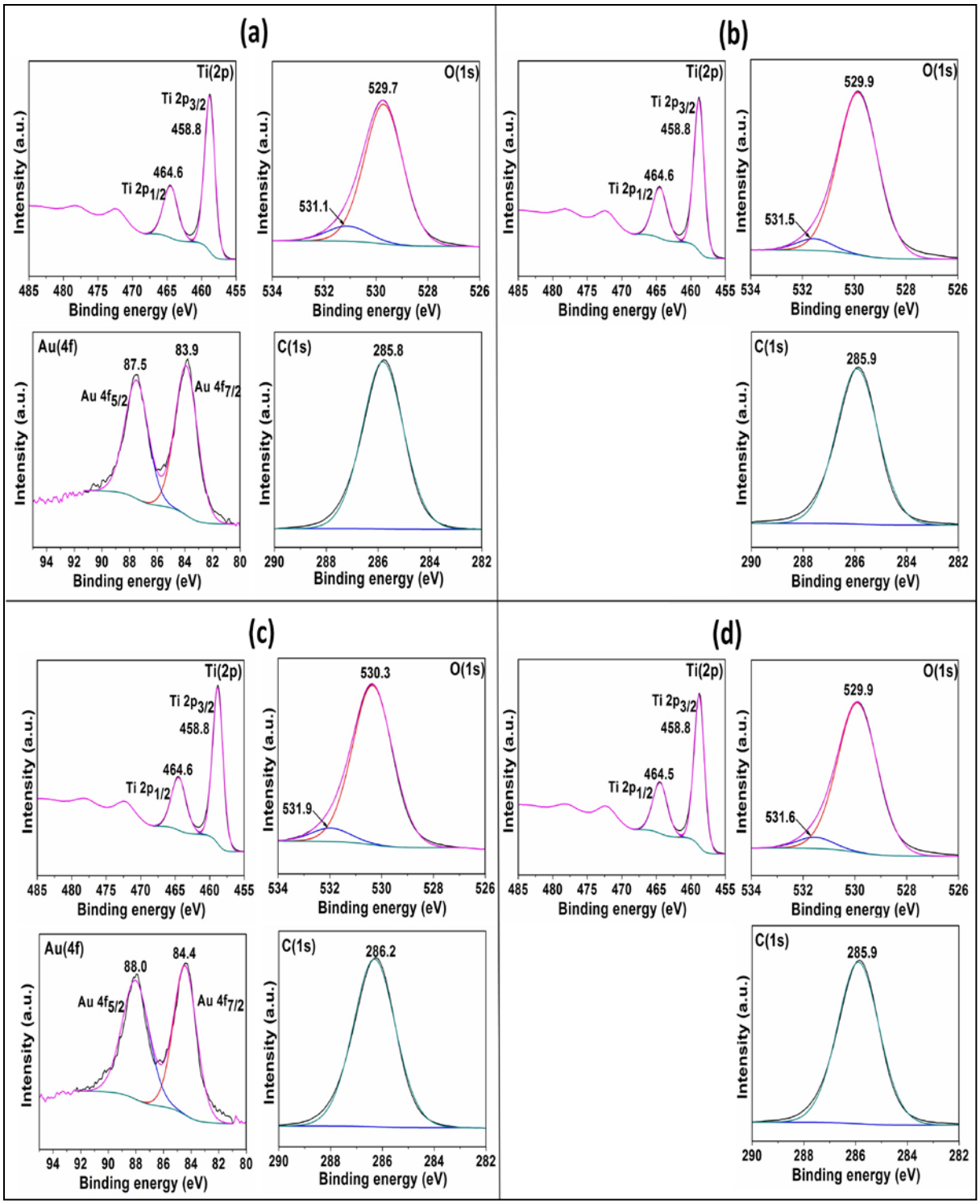

Figure 8. XPS spectra of (a) Au-HP25-600, (b) HP25-600, (c) Au-SGH-600 and (d) SGH-600.

Table 3. XPS analysis and BET surface area and pore volume.

Photocatalysts	Ti(*2p*) atomic %	O(*1s*) atomic %	C(*1s*) atomic %	Au(*4f*) atomic %	BET surface area $m^2 \cdot g^{-1}$	Pore volume $cm^3 \cdot g^{-1}$
HP25-600	15.87	40.09	44.04	--	21.85	0.0601
Au-HP25-600	16.84	37.52	45.43	0.21	22.30	0.0753
SGH-600	17.45	39.24	43.31	--	23.12	0.0749
Au-SGH-600	17.10	38.37	44.36	0.19	24.16	0.0809

3.7 Photocatalytic activity

The results of the photocatalytic activity tests for the HP25 and SGH photocatalyst series are shown in Figures 9 and 10, respectively. In both cases, the concentration profiles are shown of the pollutant 2,4-D, the toxic intermediate 2,4-DCP and chloride ions, as well as the evolution over time of the relative concentration of organic carbon during 120 min of illumination.

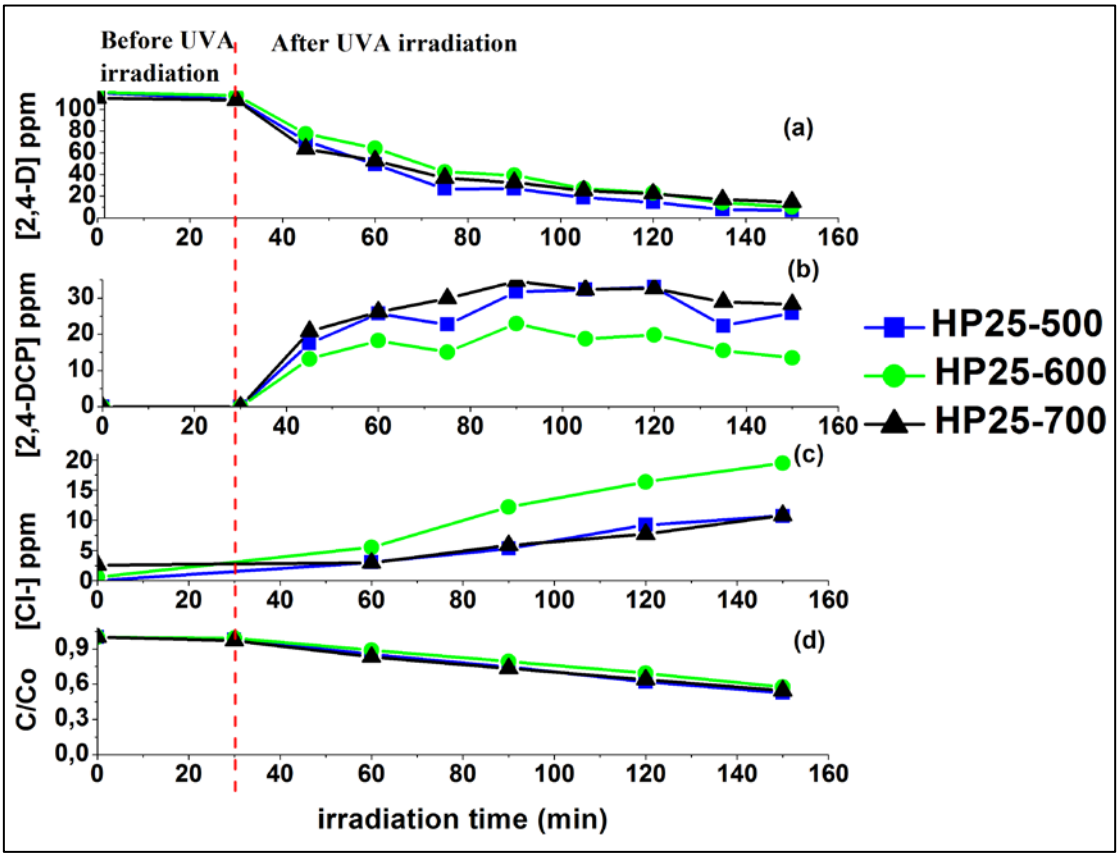

Figure 9. (a) *2,4*-Dichlorophenoxyacetic acid degradation, (b) Intermediate 2,4-DCP formed, (c) Cl^- formed, (d) total degree of mineralization with HP25 nanobelt series calcined at 500°C-600°C-700°C.

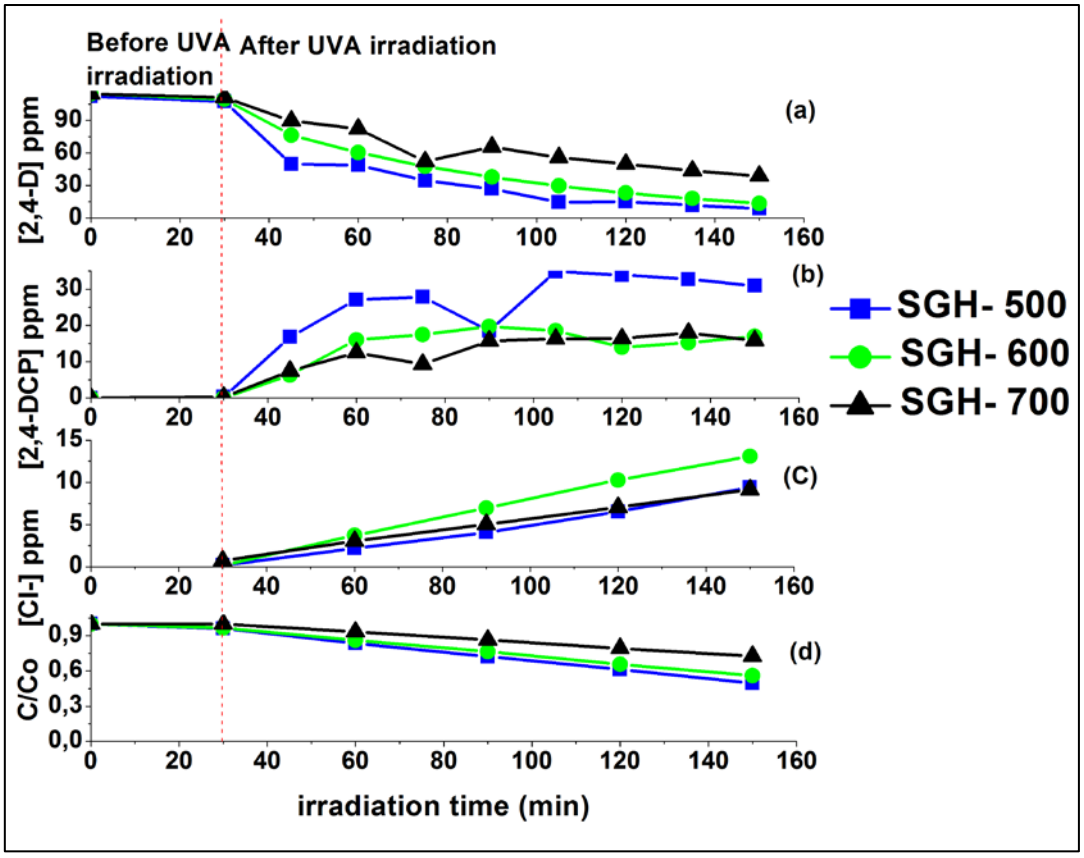

Figure 10. (a) *2,4*-Dichlorophenoxyacetic acid degradation, (b) intermediate 2,4-DCP formed, (c) Cl^- formed, (d) total degree of mineralization with SGH nanobelt series calcined at 500°C-600°C-700°C.

It can be observed that photocatalytic degradation performance decreased gradually with increasing calcination temperature and followed the order for HP25 catalysts calcined at 500°C, 600°C, and 700°C (93.99%, 91.45% and 86.74%, respectively).

A similar tendency was seen in the SGH series, but with a decrease in degradation of 2,4-D compared to the HP25 series. The values obtained were 90.84%, 88.33% and 66.23% for SGH catalysts calcined at 500°C, 600°C and 700°C, respectively.

The simplified and integrated Langmuir-Hinshelwood (L-H) kinetic model (simplified in that the product of the adsorption constant and concentration is much lower than 1) is generally used to fit the concentration profile of pollutants in heterogeneous photocatalysis [40]:

$$\ln\left(\frac{C_0}{C}\right) = k \cdot t$$

C_0: The adsorption equilibrium concentration of 2,4-D.

C: concentration of 2,4-D at time t.

k: Apparent rate constant.

Table 4 shows the values of the apparent constant of the 2,4-D degradation rate calculated from the slopes obtained from the first order integrated kinetic equation. These constants follow the same tendency as the degradation percentages.

Mineralization was evaluated in terms of TOC removal. It was observed that TOC follows an apparent zero kinetic order in the first two hours of photoactivity. In the SGH series, TOC removal followed a similar pattern, decreasing with increasing calcination temperature. However, this behavior differed in the HP25 series, where it remained almost constant, with no increased temperature effect. It is clear that in the two series of TiO_2 nanobelts, the maximum TOC % removal values corresponded to TiO_2 nanobelt catalysts calcined at 500°C (46.78% and 44.20% after 120 min for HP25-500 and SGH-500, respectively).

Table 4. Percentage of TOC removal and apparent rate constant (min^{-1}) of photocatalytic degradation of 2,4-D.

Photocatalyst	**TOC/%**	***k*/min^{-1}**	**Photocatalyst**	**TOC/%**	***k*/min^{-1}**
HP25-500	46.78	0.020	**SGH-500**	44.20	0.017
HP25-600	42.39	0.017	**SGH-600**	43.97	0.015
HP25-700	45.50	0.014	**SGH-700**	27.32	0.007

According to the photocatalytic activity results, it could be inferred that the TiO_2 nanobelts calcined at 500°C with pure TiO_2(B) phase exhibit the highest photocatalytic capacity. However, more useful information was required on chloride ion production in the reaction (for instance, whether the chloride ion concentration attains the stoichiometric value) and the intermediates of 2,4-D formed during the treatment.

3.7.1 Identification and time-evolution of intermediate and chloride ions

The 2,4-D degradation by-products were determined by HPLC. The results indicate that during degradation of 2,4-D, the more toxic intermediate, 2,4-DCP, was formed in all cases. This intermediate occurs as a result of the attack of the $^{\bullet}OH$ radical on the C-O bond of the phenoxy group of the 2,4-D molecule. Another intermediate, chlorohydroquinone (CHQ), was generated via a dechlorination reaction in which a chlorine atom of 2,4-DCP situated in *para* position was replaced by an $^{\bullet}OH$ radical [8]. A small amount of 2,4-DCP isomer, as 2,6-DCP, and the minor intermediate *4*-chlorocatechol (4-CHC) were also detected. The degradation pathway of 2,4-D was similar to that reported in other publications [8,41,42] .

Figures 6(c) and 7(c) show that the maximum conversion of chloride ions formed in solution was 52.7% and 35.34% for HP25 and SGH, respectively, calcined at 600°C. Moreover, these two catalysts are characterized by their lower production of 2,4-DCP which is considered more toxic than the initial pollutant 2,4-D [1]. Based on these results, it could be

inferred that HP25 and SGH calcined at 500°C and 700°C are not the optimum catalysts if compared to the HP25 and SGH catalysts calcined at 600°C which contain TiO_2(B)/anatase mixed phases.

3.7.2 Effect of loaded Au nanoparticles

In accordance with the results given in the previous section, nanobelt samples calcined at 600°C were selected as the best photocatalyst, and so were chosen for surface photodeposition with gold nanoparticles.

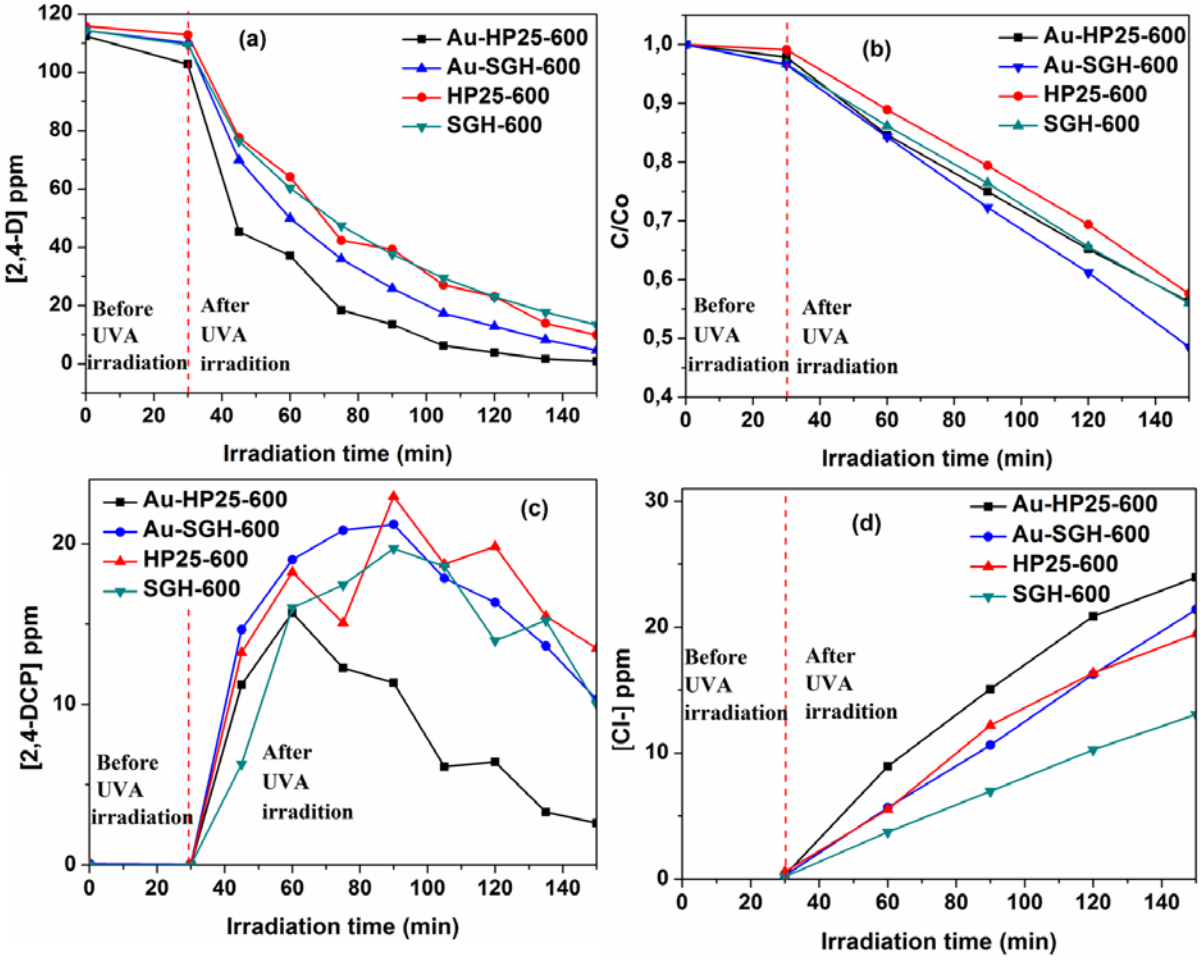

Figure 11. (a) Concentration profile of 2,4-D, (b) Temporal evolution of relative TOC (degree of mineralization), (c) Concentration profile of 2,4-DCP (intermediate) and (d) Temporal evolution of chloride ions.

Figure 11 shows the 2,4-D concentration profile (a), degree of mineralization (b), 2,4-DCP intermediate temporal evolution (c), and chloride ion temporal evolution. With both photocatalyst series, photocatalytic activity was higher with TiO_2 nanobelts and Au nanoparticles than with bare TiO_2 nanobelts. These results could be due to the formation of a potential energy barrier for electrons formed at a metal-semiconductor junction during the scattering of the Au nanoparticles on the surface of the TiO_2 nanobelts. This barrier formation may affect the interfacial charge-transfer and reduce the e^-/h^+ recombination rate in

photocatalysis. This is an important process in the performance of metal-semiconductor heterostructures and induces an enhancement of photocatalytic activity [24].

As depicted in Figure 11(a), catalytic performance of the TiO_2 nanobelt increased with Au incorporation. 2,4-D degradation reached 99.2% and 95.91% for the Au-HP25-600 and Au-SGH-600 nanobelts, respectively.

It can be seen in Figure 11 (c) and (d) that chloride ion growth formed in the solution using Au-HP25-600 and Au-SGH-600 was better than that of the bare photocatalysts HP25-600 and SGH-600, increasing to 64.5% and 57.81%, respectively. Thus, the formation of toxic intermediates was lower after Au incorporation, as can be especially observed for the HP25-600 in Figure 11(c).

Mineralization was subsequently followed for longer times of 4 h. It was observed that 90% mineralization was attained after Au incorporation compared to 61% for the HP25-600 and 71% for the SGH-600. The increase in activity was therefore greater for the HP25.

It should be noted that, in the case of the HP25-600 and Au-HP25-600 of mixed TiO_2(B)/anatase phase, there is a predominance of anatase phase at around 63.5%. Both photocatalysts have high photocatalytic efficiency. However, when TiO_2(B) is the predominant phase (as is the case with SGH-600 and Au-SGH-600 with 66.9% of TiO_2(B) and 33.1% anatase) there is lower photocatalytic activity efficiency [32] than when anatase is the predominant phase. This may be interpreted as the result of better separation of the charge carriers, which can be attributed to the rich anatase phase leading to facilitation of the interfacial transfer of electrons between the two phases from the conduction band of TiO_2(B) to anatase and reduction of the e^-/h^+ recombination center. This is confirmed by other studies with different anatase/rutile [43], and TiO_2(B)/anatase [32] mixtures. It can be argued that TiO_2(B) plays a similar role to that of rutile [33].

A schematic representation of the degradation mechanism of 2,4-D is shown in Scheme 2. In the literature it has been reported that the conduction and valence band potentials in TiO_2(B) are higher than in anatase [39,44]. The charge transfer process from the photogenerated holes stimulated in anatase toward the TiO_2(B) phase due to the higher valence band edge potentials subsequently oxidizes compounds present in the medium. The photoinduced electrons of the conduction band of TiO_2(B) migrate to the anatase phase owing to a lower conduction band potential. Also, the noble metal Au particles trap the photoinduced electrons generated in the conduction bands and prevent their return through the Schottky barrier formed between Au and TiO_2. This interface is beneficial because it contributes to reducing the electron-hole recombination rate and improves photocatalytic performance.

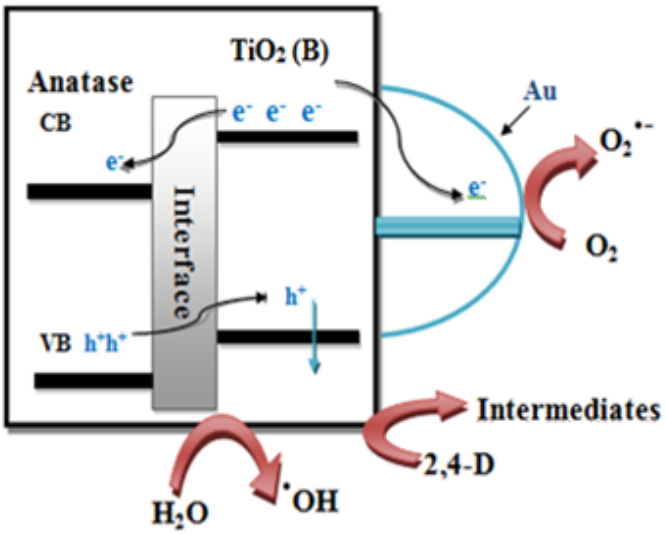

Scheme 2. Mechanism of the degradation of 2,4-D by Au-(TiO_2(B)-Anatase) nanobelts under UVA irradiation.

3.7.3 Toxicity results

Table 5. Toxicity results of degradation of 2,4-D at different irradiation times with HP25-600, Au-HP25-600, SGH-600, and Au-SGH-600.

	Inhibition %			
Time	**Au-HP25-600**	**Au-SGH-600**	**HP25-600**	**SGH-600**
0 min	46.73	45.98	30.05	36.33
60 min	97.92	99.15	84.08	97.78
120 min	91.83	87.81	93.71	98.76
180 min	16.06	75.82	81.66	98.23
240 min	OFF Curve (Very low)	OFF Curve (Very low)	10.77	61.67

Finally, as 2,4-DCP, the main intermediate, or other organochlorides which are formed in the mineralization, are more toxic than the initial pollutant, 2,4-D [1], a toxicity study was carried out to obtain toxicological information on 2,4-D and its intermediates. For this purpose, the marine bioluminescent bacteria *Vibrio fischeri* was used, with the test based on inhibition of bioluminescence.

As can be seen in Table 5, all the samples showed the same tendency of a strong increase in inhibition compared to the initial value, followed by a fall in inhibition. The lowest toxicity value for 180 min was obtained with the Au-HP25-600, with this being the catalyst for which the 2,4-D attains its maximum value (15 ppm) at 30 min before rapidly decreasing. For the other catalysts, toxicity continues to be high at 180 min as there are still very high concentrations (12 ppm) of 2,4-DCP after 120 min of illumination. Even so, it can be seen how the improvement produced by the presence of Au results in insignificant toxicity after 240 min, which contrasts with the still higher than 10% toxicity values for the HP25-600 and SGH-600.

4. Conclusions

This study considers photodegradation of the herbicide *2,4*-dichlorophenoxyacetic acid with different TiO_2 nanobelt structures: TiO_2(B)/anatase mixed phases, pure TiO_2(B) and pure anatase. Two series of photocatalysts were generated with hydrothermal reaction using two different TiO_2 nanoparticles: commercial P25 (HP25 series) and amorphous home-made TiO_2 (SGH series). The initial TiO_2 material for nanobelt synthesis plays an essential role in phase transformation. With P25 as the initial material, the transformation from monoclinic to anatase phase in the nanobelts is faster than with the SG material: HP25-600 has 64% anatase and 36% TiO_2(B), whereas with SGH-600 the ratio is inverted.

The impact of the TiO_2 nanobelt structure on photocatalytic activity was studied with and without deposition of gold (Au).

The anatase-rich Au-HP25-600(TiO_2(B)/anatase) nanobelt photocatalyst produced higher degradation of 2,4-D (99.2%) compared to the TiO_2(B)-rich Au-SGH-600(TiO_2(B)/anatase) (95%) and performed better than bare TiO_2 nanobelts.

In addition, the photocatalytic performance of the Au-HP25-600, particularly in terms of detoxification, would seem to indicate that a biphasic nanobelt structure (TiO_2(B)/anatase) with anatase as predominant phase may be considered a good support for the incorporation of gold nanoparticles and hence improved photocatalytic activity. The Au nanoparticles act as a trap for the photoinduced electrons generated in the conduction bands and prevent their return through the Schottky barrier transformed between Au and TiO_2 nanobelts, thereby contributing to reducing electron-hole recombination and improving photocatalytic performance.

Acknowledgements

We are grateful for the financial support of the Spanish Ministry of Economy and Competitiveness through the projects CTQ2015-64664-C2-1-P and of the Canary Islands Agency for Research, Innovation and the Information Society (ACIISI) of the Canary Islands Government through the FANOX Project (PROID2017010034). We would also like to thank the Spanish Ministry of Science and Innovation for the UNLP10-3E-726 infrastructure, co-financed with ERDF funds. Asma Chenchana would like to express gratitude for the mobility grant awarded under the UNetBA Erasmus Program. We are also grateful for the expert advice offered by Davinia Garzón Sousa with respect to acquisition of the infrared spectra.

References

[1] C. Yu, H. Wang, X. Liu, X. Quan, S. Chen, J. Zhang, P. Zhang, Photodegradation of 2,4-D induced by NO2-in aqueous solutions: The role of NO2, J. Environ. Sci. (China). 26 (2014) 1383–1387. doi:10.1016/j.jes.2014.05.002.

[2] E.I. Seck, J.M. Doña-Rodríguez, C. Fernández-Rodríguez, O.M. González-Díaz, J. Araña, J. Pérez-Peña, Photocatalytic removal of 2,4-dichlorophenoxyacetic acid by using sol-gel synthesized nanocrystalline and commercial TiO2: Operational parameters optimization and toxicity studies, Appl. Catal. B Environ. 125 (2012) 28–34. doi:10.1016/j.apcatb.2012.05.028.

[3] K. Djebbar, T. Sehili, Kinetics of heterogeneous photocatalytic decomposition of 2,4-dichlorophenoxyacetic acid over titanium dioxide and zinc oxide in aqueous solution, Pestic. Sci. 54

(1998) 269–276. doi:10.1002/(SICI)1096-9063(1998110)54:3<269::AID-PS811>3.0.CO;2-I.
[4] Q. Chen, H. Liu, Y. Xin, X. Cheng, TiO2 nanobelts - Effect of calcination temperature on optical, photoelectrochemical and photocatalytic properties, Electrochim. Acta. 111 (2013) 284–291. doi:10.1016/j.electacta.2013.08.049.
[5] L. Yang, W. Sun, S. Luo, Y. Luo, White fungus-like mesoporous Bi2S3ball/TiO2heterojunction with high photocatalytic efficiency in purifying 2,4-dichlorophenoxyacetic acid/Cr(VI) contaminated water, Appl. Catal. B Environ. 156–157 (2014) 25–34. doi:10.1016/j.apcatb.2014.02.044.
[6] J. Dai, J. Yang, X. Wang, L. Zhang, Y. Li, Enhanced visible-light photocatalytic activity for selective oxidation of amines into imines over TiO_2(B)/anatase mixed-phase nanowires, Appl. Surf. Sci. 349 (2015) 343–352. doi:10.1016/j.apsusc.2015.04.232.
[7] Q. Xu, Y. Ma, J. Zhang, X. Wang, Z. Feng, C. Li, Enhancing hydrogen production activity and suppressing CO formation from photocatalytic biomass reforming on Pt/TiO2 by optimizing anatase-rutile phase structure, J. Catal. 278 (2011) 329–335. doi:10.1016/j.jcat.2011.01.001.
[8] H. Chen, Z. Zhang, Z. Yang, Q. Yang, B. Li, Z. Bai, Heterogeneous Fenton-like catalytic degradation of 2,4-dichlorophenoxyacetic acid in water with FeS, Chem. Eng. J. 273 (2015) 481–489. doi:10.1016/j.cej.2015.03.079.
[9] A.A. Vega, G.E. Imoberdorf, M. Mohseni, Photocatalytic degradation of 2,4-dichlorophenoxyacetic acid in a fluidized bed photoreactor with composite template-free TiO2photocatalyst, Appl. Catal. A Gen. 405 (2011) 120–128. doi:10.1016/j.apcata.2011.07.033.
[10] Y. Tang, S. Luo, Y. Teng, C. Liu, X. Xu, X. Zhang, L. Chen, Efficient removal of herbicide 2,4-dichlorophenoxyacetic acid from water using Ag/reduced graphene oxide co-decorated TiO_2 nanotube arrays, J. Hazard. Mater. 241–242 (2012) 323–330. doi:10.1016/j.jhazmat.2012.09.050.
[11] Q. Cai, Y. Li, L. wang, Q. Li, J. Xu, B. Gao, X. Zhang, K. Huo, P.K. Chu, Freestanding hollow double-shell Se@CNxnanobelts as large-capacity and high-rate cathodes for Li-Se batteries, Nano Energy. 32 (2017) 1–9. doi:10.1016/j.nanoen.2016.12.010.
[12] D. Chao, X. Xia, J. Liu, Z. Fan, C.F. Ng, J. Lin, H. Zhang, Z.X. Shen, H.J. Fan, A V2O5/conductive-polymer core/shell nanobelt array on three-dimensional graphite foam: A high-rate, ultrastable, and freestanding cathode for lithium-ion batteries, Adv. Mater. 26 (2014) 5794–5800. doi:10.1002/adma.201400719.
[13] X. Fang, Y. Bando, M. Liao, U.K. Gautam, C. Zhi, B. Dierre, B. Liu, T. Zhai, T. Sekiguchi, Y. Koide, D. Golberg, Single-crystalline ZnS nanobelts as ultraviolet-light sensors, Adv. Mater. 21 (2009) 2034–2039. doi:10.1002/adma.200802441.
[14] L. Li, S. Yang, F. Han, L. Wang, X. Zhang, Z. Jiang, A. Pan, Optical sensor based on a single CdS nanobelt., Sensors (Basel). 14 (2014) 7332–7341. doi:10.3390/s140407332.
[15] S. Sun, P. Gao, Y. Yang, P. Yang, Y. Chen, Y. Wang, N-Doped TiO_2 Nanobelts with Coexposed (001) and (101) Facets and Their Highly Efficient Visible-Light-Driven Photocatalytic Hydrogen Production, ACS Appl. Mater. Interfaces. 8 (2016) 18126–18131. doi:10.1021/acsami.6b05244.
[16] W. Zhou, D. Hou, Y. Sang, S. Yao, J. Zhou, G. Li, L. Li, H. Liu, S. Chen, MoO2 nanobelts@nitrogen self-doped MoS2 nanosheets as effective electrocatalysts for hydrogen evolution reaction, J. Mater. Chem. A. 2 (2014) 11358–11364. doi:10.1039/c4ta01898b.
[17] M. Harilal, S.G. Krishnan, B.L. Vijayan, M. Venkatashamy Reddy, S. Adams, A.R. Barron, M.M. Yusoff, R. Jose, Continuous nanobelts of nickel oxide–cobalt oxide hybrid with improved capacitive charge storage properties, Mater. Des. 122 (2017) 376–384. doi:10.1016/j.matdes.2017.03.024.
[18] M. Lee, S.K. Balasingam, H.Y. Jeong, W.G. Hong, H.B.R. Lee, B.H. Kim, Y. Jun, One-step hydrothermal synthesis of Graphene decorated V2O5 nanobelts for enhanced electrochemical energy storage, Sci. Rep. 5 (2015) 1–8. doi:10.1038/srep08151.
[19] L. Zhang, L. Fan, Z. Li, E. Shi, X. Li, H. Li, C. Ji, Y. Jia, J. Wei, K. Wang, H. Zhu, D. Wu, A. Cao, Graphene-CdSe nanobelt solar cells with tunable configurations, Nano Res. 4 (2011) 891–900. doi:10.1007/s12274-011-0145-6.
[20] K. Pan, Y. Dong, C. Tian, W. Zhou, G. Tian, B. Zhao, H. Fu, TiO2-B narrow nanobelt/TiO2 nanoparticle composite photoelectrode for dye-sensitized solar cells, Electrochim. Acta. 54 (2009) 7350–7356. doi:10.1016/j.electacta.2009.07.065.
[21] G. Chen, S. Ji, Y. Sang, S. Chang, Y. Wang, P. Hao, J. Claverie, H. Liu, G. Yu, Synthesis of scaly Sn3O4/TiO2 nanobelt heterostructures for enhanced UV-visible light photocatalytic activity, Nanoscale. 7 (2015) 3117–3125. doi:10.1039/c4nr05749j.
[22] J. Long, S. Wang, H. Chang, B. Zhao, B. Liu, Y. Zhou, W. Wei, X. Wang, L. Huang, W. Huang, Bi2MoO6nanobelts for crystal facet-enhanced photocatalysis, Small. 10 (2014) 2791–2795. doi:10.1002/smll.201302950.
[23] E.P. Melián, O.G. Díaz, A.O. Méndez, C.R. López, M.N. Suárez, J.M.D. Rodríguez, J.A. Navío, D.F. Hevia, J.P. Peña, Efficient and affordable hydrogen production by water photo-splitting using TiO2-

based photocatalysts, Int. J. Hydrogen Energy. 38 (2013) 2144–2155.
[24] W. Zhou, G. Du, P. Hu, G. Li, D. Wang, H. Liu, J. Wang, R.I. Boughton, D. Liu, H. Jiang, Nanoheterostructures on TiO2nanobelts achieved by acid hydrothermal method with enhanced photocatalytic and gas sensitive performance, J. Mater. Chem. 21 (2011) 7937–7945. doi:10.1039/c1jm10588d.
[25] J.A. Ortega Méndez, C.R. López, E. Pulido Melián, O. González Díaz, J.M. Doña Rodríguez, D. Fernández Hevia, M. Macías, Production of hydrogen by water photo-splitting over commercial and synthesised Au/TiO2 catalysts, Appl. Catal. B Environ. 147 (2014) 439–452. doi:10.1016/j.apcatb.2013.09.029.
[26] S.P. Tandon, J.P. Gupta, Measurement of Forbidden Energy Gap of Semiconductors by Diffuse Reflectance Spectra, Phys. Status Solidi B. (1970). doi:10.1002/pssb.19700380136.
[27] W. Zhou, L. Gai, P. Hu, J. Cui, X. Liu, D. Wang, G. Li, H. Jiang, D. Liu, H. Liu, J. Wang, Phase transformation of TiO2 nanobelts and TiO 2(B)/anatase interface heterostructure nanobelts with enhanced photocatalytic activity, CrystEngComm. 13 (2011) 6643–6649. doi:10.1039/c1ce05638g.
[28] J. Soria, J. Sanz, I. Sobrados, J.M. Coronado, M.D. Hernández-Alonso, F. Fresno, Water-Hydroxyl Interactions on Small Anatase Nanoparticles Prepared by the Hydrothermal Route, J. Phys. Chem. (2010) 16534–16540. http://pubs.acs.org/doi/abs/10.1021/jp105131w.
[29] C.H.R. A.A. Davydov, Infrared spectroscopy of adsorbed species on the surface of transition metal oxides, New York, Wiley, 1990.
[30] M. Shaban, A.M. Ashraf, M.R. Abukhadra, TiO2 Nanoribbons/Carbon Nanotubes Composite with Enhanced Photocatalytic Activity; Fabrication, Characterization, and Application, Sci. Rep. 8 (2018) 781. doi:10.1038/s41598-018-19172-w.
[31] the A.& E.R. Unit, University of Hertfordshire for a variety of end users to support risk assessments and risk management., (2007). http://sitem.herts.ac.uk/aeru/footprint/es/index.htm (accessed March 2, 2007).
[32] T.A. Kandiel, A.Y. Ahmed, D. Bahnemann, TiO 2 (B)/anatase heterostructure nanofibers decorated with anatase nanoparticles as efficient photocatalysts for methanol oxidation, J. Mol. Catal. A Chem. 425 (2016) 55–60. doi:10.1016/j.molcata.2016.09.017.
[33] Z. Zheng, H. Liu, J. Ye, J. Zhao, E.R. Waclawik, H. Zhu, Structure and contribution to photocatalytic activity of the interfaces in nanofibers with mixed anatase and TiO2(B) phases, J. Mol. Catal. A Chem. 316 (2010) 75–82. doi:10.1016/j.molcata.2009.10.002.
[34] J.A. Ortega Méndez, C.R. López, E. Pulido Melián, O. González Díaz, J.M. Doña Rodríguez, D. Fernández Hevia, M. Macías, Production of hydrogen by water photo-splitting over commercial and synthesised Au/TiO2 catalysts, Appl. Catal. B Environ. 147 (2014) 439–452. doi:10.1016/j.apcatb.2013.09.029.
[35] O. Rosseler, M. V Shankar, M. Karkmaz-Le Du, L. Schmidlin, N. Keller, V. Keller, Solar light photocatalytic hydrogen production from water over Pt and Au/TiO2 (anatase/rutile) photocatalysts: Influence of noble metal and porogen promotion, J. Catal. 269 (2010) 179–190.
[36] Y. Li, T. Li, J. Tian, X. Wang, H. Cui, TiO 2 Nanobelts Decorated with In 2 S 3 Nanoparticles as Photocatalysts with Enhanced Full-Solar-Spectrum (UV-vis-NIR) Photocatalytic Activity toward the Degradation of Tetracycline, Part. Part. Syst. Charact. 34 (2017) 1700127. doi:10.1002/ppsc.201700127.
[37] J. Tian, Y. Leng, Z. Zhao, Y. Xia, Y. Sang, P. Hao, J. Zhan, M. Li, H. Liu, Carbon quantum dots/hydrogenated TiO2 nanobelt heterostructures and their broad spectrum photocatalytic properties under UV, visible, and near-infrared irradiation, Nano Energy. 11 (2015) 419–427. doi:10.1016/j.nanoen.2014.10.025.
[38] M. Tahir, B. Tahir, N.A.S. Amin, Gold-nanoparticle-modified TiO2nanowires for plasmon-enhanced photocatalytic CO2reduction with H2under visible light irradiation, Appl. Surf. Sci. 356 (2015) 1289–1299. doi:10.1016/j.apsusc.2015.08.231.
[39] T. Jiang, C. Jia, L. Zhang, S. He, Y. Sang, H. Li, Y. Li, X. Xu, H. Liu, Gold and gold-palladium alloy nanoparticles on heterostructured TiO2nanobelts as plasmonic photocatalysts for benzyl alcohol oxidation, Nanoscale. 7 (2015) 209–217. doi:10.1039/c4nr05905k.
[40] S. Ghasemi, S.R. Setayesh, A. Habibi-Yangjeh, M.R. Hormozi-Nezhad, M.R. Gholami, Assembly of CeO 2-TiO 2 nanoparticles prepared in room temperature ionic liquid on graphene nanosheets for photocatalytic degradation of pollutants, J. Hazard. Mater. 199–200 (2012) 170–178. doi:10.1016/j.jhazmat.2011.10.080.
[41] Z. Yang, X. Xu, M. Dai, L. Wang, X. Shi, R. Guo, Rapid degradation of 2,4-dichlorophenoxyacetic acid facilitated by acetate under methanogenic condition, Bioresour. Technol. 232 (2017) 146–151. doi:10.1016/j.biortech.2017.01.069.
[42] A. V Schenone, L.O. Conte, M.A. Botta, O.M. Alfano, Modeling and optimization of photo-Fenton degradation of 2,4-D using ferrioxalate complex and response surface methodology (RSM), J. Environ. Manage. 155 (2015) 177–183. doi:10.1016/j.jenvman.2015.03.028.

[43] T.A. Kandiel, R. Dillert, A. Feldhoff, D.W. Bahnemann, Direct synthesis of photocatalytically active rutile TiO2nanorods partly decorated with anatase nanoparticles, J. Phys. Chem. C. 114 (2010) 4909–4915. doi:10.1021/jp912008k.

[44] H.-H. Lo, N.O. Gopal, S.-C. Sheu, S.-C. Ke, Electron Paramagnetic Resonance Investigation of Charge Transfer in TiO 2 (B)/Anatase and N–TiO 2 (B)/Anatase Mixed-Phase Nanowires: The Relative Valence and Conduction Band Edges in the Two Phases, J. Phys. Chem. C. 118 (2014) 2877–2884. doi:10.1021/jp411723m.